Volume 1 | Number 1 | Jan 2013 | Pages 1–100

Journal of
Materials Chemistry A

Materials for energy and sustainability
www.rsc.org/materialsA

ROYAL SOCIETY
OF CHEMISTRY

ROYAL SOCIETY
OF CHEMISTRY

www.rsc.org/materialsA

The pivotal role of the dopant choice on the thermodynamics of hydration and associations in proton conducting $BaCe_{0.9}X_{0.1}O_{3-\delta}$ (X = Sc, Ga, Y, In, Gd and Er)

Andreas Løken, Tor Svendsen Bjørheim and Reidar Haugsrud

Department of Chemistry, University of Oslo, FERMiO, Gaustadalléen 21, NO-0349 Oslo, Norway

A B S T R A C T

The choice of acceptor has been demonstrated to result in distinctly different hydration properties in proton conducting perovskites such as $BaZrO_3$ and $BaCeO_3$ and may as such have detrimental implications for their proton conductivity. The underlying causes for these differences are, however, still not understood. The following contribution elucidates the variations in the thermodynamics of hydration and associations in acceptor doped $BaCeO_3$ where the dopants have been chosen to encompass a wide range of ionic radii and electronegativities. This is accomplished by comprehensive thermogravimetric (TG) measurements and first principles calculations (DFT), allowing correlations of hydration properties to atomistic material properties to be drawn. The results obtained from both techniques are in excellent agreement and demonstrate that the hydration enthalpy becomes more exothermic with an increasing ionic character of the acceptor-oxygen bond. The defect structure of all studied compositions is furthermore dominated by complexes between the acceptors and oxygen vacancies or protons. The presence of such complexes will for instance severely inhibit the proton conductivity due to higher activation energies and the implications of acceptor-defect associates on proton concentration limits, ionic transport and hydration properties are addressed and discussed.

1. Introduction

The functional properties of many materials can be tailored by either acceptor or donor doping, which increases the concentration of positively or negatively charged defects, respectively. For ABO_3 perovskites, acceptor doping can for instance be achieved by substituting a lower valent cation onto the B-site. The resulting positively charged defects and their concentrations will depend on atmospheric conditions, temperature and the band gap of

the material. Under dry conditions, oxygen vacancies ($v_O^{\bullet\bullet}$) and/or electron holes ($h^{\bullet}$) are generally the dominating effectively positive defects whereas protons ($OH_O^{\bullet}$) may come into play in the presence of water vapour. The formation and concentration of protons in an acceptor doped wide band gap perovskite oxide can generally be described by the equilibrium between oxygen vacancies and protons (hydration reaction) and its associated equilibrium constant (K_{hydr}):

$$H_2O(g) + v_O^{\bullet\bullet} + O_O^{\times} \rightleftharpoons 2OH_O^{\bullet} \tag{1}$$
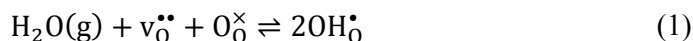
$$K_{hydr} = \frac{[OH_O^{\bullet}]^2}{[v_O^{\bullet\bullet}][O_O^{\times}]p_{H_2O}} = \exp\left(-\frac{\Delta_{hydr}H^{\circ}}{RT}\right)\exp\left(\frac{\Delta_{hydr}S^{\circ}}{R}\right) \tag{2}$$

where $\Delta_{hydr}H^{\circ}$ and $\Delta_{hydr}S^{\circ}$ are the standard hydration enthalpy and entropy, respectively. Efforts have been made to correlate the enthalpy and entropy of hydration to other material parameters such as ionic radii (R) and electronegativities (χ)[1,2]. These empirical correlations account for the general variations in hydration properties between materials, but poorly describe the changes when varying the amount of, or even the choice of acceptor[3,4].

In this contribution, we will address effects of the choice of acceptor on the hydration thermodynamics by investigating $BaCe_{0.9}X_{0.1}O_{3-\delta}$ where X = Sc, Ga, Y, In, Gd and Er by thermogravimetry (TG) and first principles calculations (DFT). All measurements are carried out in the same manner and interpreted with the same defect chemical model. By supporting the TG results with first principles calculations, we will look beyond electronegativities and ionic radii towards the ionicity and covalency of the bonds within each material system aiming to comprehend the hydration trends observed. As the current contribution presents the first systematic combined TG/DFT study of the hydration thermodynamics of $BaCe_{0.9}X_{0.1}O_{3-\delta}$, the available literature on hydration trends and proton concentration limits will briefly be discussed.

Hydration trends with different dopants

To reach high solubility, the acceptors should ideally resemble the host cation and are therefore chosen based on e.g. similarity in ionic radius (R) and electronegativity (χ). These

physical properties have also been suggested as correlation parameters for the hydration thermodynamics of ABO_3 perovskites e.g. by Norby et $al.$[1,2]: $\Delta_{hydr}H^\circ$ generally becomes more exothermic when the electronegativity difference between the B- and A-site cation, χ_{B-A}, diminishes, and when the Goldschmidt tolerance factor, t (directly related to the radius of the A- and B-site cation), decreases. For $\Delta_{hydr}S^\circ$, neither of the parameters gave any clear correlations.

There is a lack of systematic studies of the effect of dopant choice on the hydration thermodynamics, and the few that exist demonstrate no clear trends with respect to material parameters. For instance, Kreuer et $al.$[4] investigated several acceptor dopants (In^{3+}, Sc^{3+}, Y^{3+} and Gd^{3+}) for $BaZrO_3$ but found no simple relationships between the hydration thermodynamics and R or χ of the dopant. In fact, the two dopants with ionic radii most similar to the host cation (Zr^{4+}), In^{3+} and Sc^{3+}, were demonstrated to exhibit entirely different hydration enthalpies; -119.4 and -66.6 kJ mol^{-1}, respectively. Oishi et $al.$[5,6] showed for $BaCe_{0.9}M_{0.1}O_{3-\delta}$ (M = Yb, Y and Nd) that the hydration enthalpy becomes less negative when the ionic radius increases in the order Yb^{3+} (0.868 Å; -127 kJ mol^{-1}) $\rightarrow$ Y^{3+} (0.9 Å; -122 kJ mol^{-1}) $\rightarrow$ Nd^{3+} (0.983 Å; -58 kJ mol^{-1}). While this preliminarily indicates that matching ionic radii to the host (Ce^{4+}, 0.87 Å) minimises the hydration enthalpy, investigations including dopants of a smaller size are needed to further support this hypothesis. Also, for $BaCe_{0.9}Nd_{0.1}O_{3-\delta}$, the concentration of protons and oxygen vacancies was shown to change as a function of p_{O_2}, which further complicates the extraction of thermodynamic parameters. Other studies have only considered a limited number of dopants or have only investigated the effects on proton conductivity, which can be cumbersome to relate back to hydration thermodynamics.

Underlying causes for limiting proton incorporation

Measured proton concentrations are often encountered to be significantly lower than the amount given by the nominal acceptor concentration, which has been particularly evident for Ba-containing perovskites[7-11]. Such limits directly influence the empirically determined hydration thermodynamic parameters and the underlying causes will therefore be discussed here. This discrepancy goes beyond a low solubility of the acceptor as there are numerous reports of high doping solubilities (up to 30 atomic%) in for instance $BaCeO_3$ which still

show limiting proton concentrations[10-12]. The low proton content in these materials has been argued to stem from BaO (g) loss, resulting in the incorporation of the dopant cation onto the A-site (Ba) where it acts as a donor, $X_{Ba}^{\bullet}$ [9, 13-15]:

$$2Ba_{Ba}^{\times} + 2O_O^{\times} + X_{Ce}^{/} + v_O^{\bullet\bullet} \rightleftharpoons X_{Ba}^{\bullet} + 2BaO(g) \qquad (3)$$
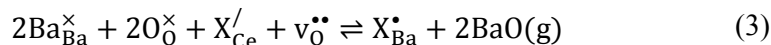
To compensate for the formation of such donors, the concentration of oxygen vacancies diminishes, which in turn decreases the proton uptake. While this defect equilibrium (3) can potentially explain discrepancies for the Ba-based materials, it cannot account for the limited proton concentration in material systems with non-volatile cations, e.g. acceptor doped $SrZrO_3$, $SrCeO_3$ and $LaYbO_3$[16-18].

The low saturation levels could instead stem from the formation of complexes between the acceptors and protons or oxygen vacancies, which may limit hydration if the acceptors trap oxygen vacancies to a larger extent than protons. Such complexes have been demonstrated experimentally and computationally for numerous perovskite oxides[14, 19-22].

2. The approaches of the study

10% acceptor doped $BaCeO_3$ is the material in focus within this contribution[20, 23]. $BaCeO_3$ displays a wide range of hydration enthalpies varying from -58 to -170 kJ mol^{-1} depending on the type and amount of dopant[6, 23-25], and, is as such, an ideal model material. It is, however, difficult to assess whether these enthalpies stem from actual dopant effects or measurement discrepancies, as large enthalpy differences exist even for the same dopant measured under similar experimental conditions[25, 26].

In order to address the limitations of the existing correlations between hydration thermodynamics and electronegativity and ionic radius, dopant elements encompassing a wide range in these two parameters have been chosen (cf. Table 1).

Table 1: The ionic radii and electronegativities in increasing order of the dopants investigated in this work along with the host cations in bold (Ba^{2+} and Ce^{4+}). The ionic radii and Allred-Rochow electronegativities are taken from Shannon *et al.*[27] and Little *et al.*[28], respectively.

Cation	Ionic Radius / Å		Species	Electronegativity (Allred-Rochow)
Ga^{3+}	0.62		**Ba**	**0.97**
Sc^{3+}	0.745		**Ce**	**1.08**
In^{3+}	0.8		Er	1.11
Ce^{4+}	**0.87**		Y	1.11
Er^{3+}	0.89		Gd	1.11
Y^{3+}	0.9		Sc	1.20
Gd^{3+}	0.938		In	1.49
Ba^{2+}	**1.61**		Ga	1.82

The limits to proton uptake will be investigated and discussed mainly on the basis of associations between the acceptor, and oxygen vacancies and protons. While most reports in literature only focus on single associate pairs i.e. $(X_{Ce}v_O)^{\bullet}$ and $(X_{Ce}OH_O)^X$, the present work also assesses larger complexes. The thermodynamics of these complexes will be addressed from DFT calculations and discussed in relation to experimentally determined proton concentration limits.

3. Experimental and theoretical techniques

3.1 Sample preparation and characterisation

$BaCe_{0.9}X_{0.1}O_{3-\delta}$ (X = Sc, Ga, Y, In, Gd and Er, hereafter BCX10) was synthesised by a traditional solid state reaction method; powder mixing followed by calcinations at 1200 and 1300 °C for 12 h (details given in the supplementary information).

3.2 Thermogravimetric methodology

Isobaric thermogravimetric (TG) measurements were conducted using a Netzsch STA 449 F1 Jupiter with a SiC furnace in wet Ar ($p_{O_2} = 10^{-5}$ and $p_{H_2O} = 0.02$ atm) in which p_{H_2O} was controlled by mixing gases flowing through KBr (aq) and over P_2O_5 (s). To promote reliable relative mass changes at the highest temperatures (T ≥ 800 °C), all measurements were carried out using alumina crucibles with sample masses of at least 2 g. Measurements were

performed as a function of temperature in the range of 1000 °C to 300 °C including an isothermal drying segment at 1100 °C. All samples were allowed to equilibrate at each temperature with a cooling rate of 5 °C min^{-1} between the isothermal steps.

High p_{H_2O} (0.1 – 1 atm) measurements were conducted using a Netzsch STA 449 C equipped with a steam generator and water vapour furnace. The measurements were conducted using Pt10Rh crucibles with 300-600 mg sample masses keeping the reference crucible consistently empty. Measurements were done isothermally, switching from 1 atm bottle dry N_2 (g) (p_{O_2} = 10^{-5} atm) to 1 atm H_2O (g) or humidified N_2 (g) (p_{H_2O} = 0.18 atm) at temperatures between 1000 and 300 °C. All samples were equilibrated in dry gas up to 30 minutes before hydration. Dehydration was performed by 30 minutes dwells at 1100 °C under 130 ml/min flow of bottle dry N_2 (g). This gas was also passed through the steam generator to ensure that the line was completely dry during dehydration. Ramp rates were 20 °C min^{-1} and 10 °C min^{-1} for heating and cooling, respectively. Additional switches from N_2 (g) to bottle dry O_2 (g) were conducted at 600 °C to address effects of oxidation.

To correct for buoyancy and drift, all measurements were repeated using empty crucibles (alumina or Pt10Rh).

3.3 Computational methodology

The first principles calculations in this work were performed within the Density Functional Theory (DFT) formalism as implemented in VASP[29] using the Generalised Gradient Approximation functional due to Perdew, Burke and Ernzerhof (GGA-PBE)[30] and the projector-augmented wave (PAW) method[31]. A constant cut-off energy of 400 eV for the plane-waves was used. All integrations over the Brillouin zone were performed using a Γ-centred 2 × 2 × 2 **k**-mesh. Experimentally determined structures were used as starting points for the calculations. As each orthorhombic *Pmcn* unit cell of $BaCeO_3$ contains 20 atoms, 2 × 2 × 2 super cells (i.e. 160 atoms) were used in all calculations. The pristine structures were optimised prior to the defect calculations by relaxing all volumes and ionic positions until the residual forces were less than 0.02 eV Å^{-1}, with an energy convergence criterion of 10^{-6} eV for self-consistency.

BaCeO$_3$ exhibits two structurally inequivalent oxygen sites; two apical oxygen sites in Wyckoff position 4c and four equatorial oxygen sites in Wyckoff position 8d. In acceptor doped BaCeO$_3$, these sites can be octahedrally coordinated to either Ce or X (acceptor dopant) cations, which thus yields four unique oxygen positions; O4c, O8f, O4cx and O8fx where x denotes an oxygen ion coordinated to the dopant. We have therefore considered oxygen vacancies and protons at all oxygen sites. Configurations with protons and oxygen vacancies in the next-nearest octahedron to the acceptor demonstrated no difference in the formation energies relative to the defects placed far away from the acceptor. The proton may take on several configurations around each O ion, and we have therefore considered four unique positions along the bisector of the two oxygen-oxygen connecting lines, in correspondence with previous work on Sc-doped SrZrO$_3$[32] (see Figure 1). This was done for all four oxygen positions, thus amounting to a total of 16 configurations.
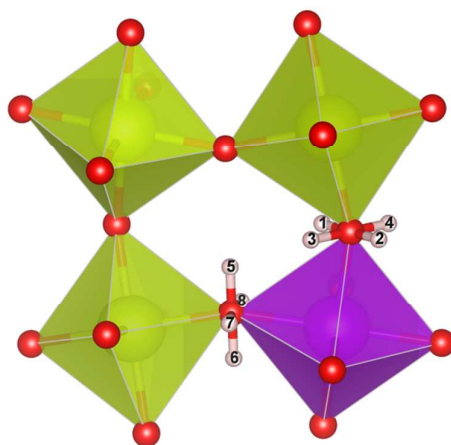

Figure 1: Schematic of eight of the proton positions around the dopant investigated for all acceptor doped BaCeO$_3$ supercells. The yellow octahedra are CeO$_6$ while the purple octahedron is GdO$_6$. 1-4 depict positions around the O4cx while 5-8 depict positions around O8dx.

For charged defects, the total charge of the cell was adjusted to simulate the desired charge state of the defects, by the standard means of charge-compensation by a homogenous jellium charge. Only a single dopant was used (unless otherwise stated) in each supercell amounting to a dopant concentration of 3.125 mol%. While this differs from the experimental doping concentrations of 10 mol%, it is chosen to minimise any dopant-dopant interactions. Also,

test calculations using up to three dopants demonstrated similar formation energies for the proton and oxygen vacancy unless the dopants were situated in neighbouring octahedra.

The enthalpies of hydration of $v_O^{\bullet\bullet}$ and associates between oxygen vacancies and acceptors, $(X_{Ce}v_O)^{\bullet}$, have for all systems been calculated according to:

$$\Delta_{hydr}H_{v_O^{\bullet\bullet}}^{\circ} = 2E_{OH_O^{\bullet}}^{tot} - E_{v_O^{\bullet\bullet}}^{tot} - E_{bulk}^{tot} - E_{H_2O}^{tot} \tag{4}$$

$$\Delta_{hydr}H_{(X_{Ce}v_O)^{\bullet}}^{\circ} = 2E_{(X_{Ce}OH_O)^x}^{tot} - E_{(X_{Ce}v_O)^{\bullet}}^{tot} - E_{bulk}^{tot} - E_{H_2O}^{tot} \tag{5}$$

where $E_{OH_O^{\bullet}}^{tot}$, $E_{v_O^{\bullet\bullet}}^{tot}$, $E_{(X_{Ce}OH_O)^x}^{tot}$ and $E_{(X_{Ce}v_O)^{\bullet}}^{tot}$ are the total energies of the defective supercells for the proton, oxygen vacancy, and the proton-acceptor and oxygen vacancy-acceptor complexes, respectively, whereas E_{bulk}^{tot} represents the total energy of the pristine supercell (with or without acceptors). $E_{H_2O}^{tot}$ is the total energy for a single water molecule as obtained from DFT.

Bader charge density analyses[33] were also performed on supercells with acceptor dopants only (i.e. no protons or oxygen vacancies) to evaluate the effect of the acceptor on the effective charges of the individual ions of the supercell.

4. Results

4.1. Hydration thermodynamics of BaCe$_{0.9}$X$_{0.1}$O$_{3-\delta}$, X= Sc, Y, In, Gd, Er) from TG measurements

Figure 2 displays the TG water uptake profiles for BCIn10 and BCGd10, conducted in wet Ar ($p_{O_2} = 3 \times 10^{-5}$ and $p_{H_2O} = 0.02$ atm) as a function of decreasing temperature. The water uptake increases with decreasing temperature (1100-300 °C) for both compositions reflecting the exothermic nature of the hydration reaction (1). The materials showed no significant mass change upon switching between 1 atm N$_2$ (g) to 1 atm O$_2$ (g), revealing that the oxygen nonstoichiometry was virtually constant. Oxidation does therefore not affect the hydration measurements, in correspondence with work done on similar BaCeO$_3$ compositions by Oishi

et al.[34]. Accordingly, electron holes are minority defects in all compositions, and oxygen vacancies and protons are the dominating positive defects.
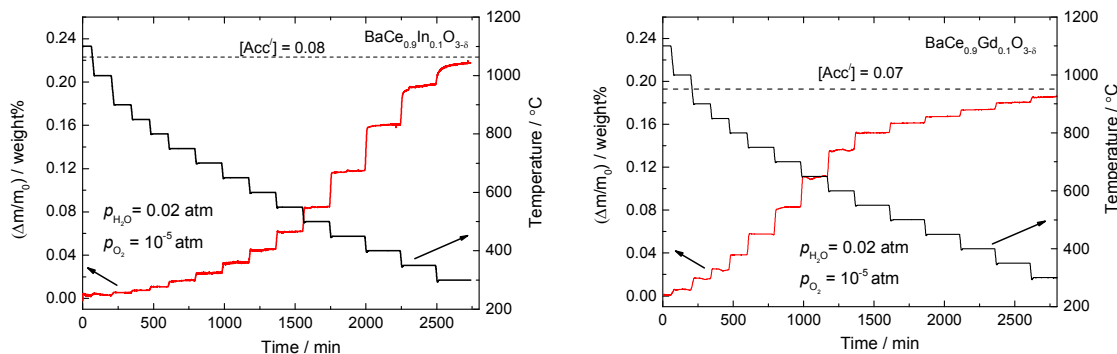

Figure 2: Thermogravimetric (TG) measurements of the water uptake for $BaCe_{0.9}In_{0.1}O_{3-\delta}$ (BCIn10) (left) and $BaCe_{0.9}Gd_{0.1}O_{3-\delta}$ (BCGd10) (right). Both measurements have been conducted in wet Ar ($p_{O_2} = 10^{-5}$ and $p_{H_2O} = 0.02$ atm) and have been corrected with a blank run where the alumina crucible was empty.

The total uptake of protons, 0.08 and 0.07 mole fractions, is lower than expected from the nominal doping level, 0.1. We have therefore defined an effective acceptor concentration $[X'_{Ce,eff}]$ giving a simplified electroneutrality along with oxygen site restriction for perovskites:

$$[X'_{Ce,eff}] = 2[v_O^{\bullet\bullet}] + [OH_O^{\bullet}] \tag{6}$$

$$[O_O^{\times}] = 3 - [v_O^{\bullet\bullet}] - [OH_O^{\bullet}] \tag{7}$$

Using these and the mass action law, the proton concentration, $[OH_O^{\bullet}]$, can be quantified in terms of the hydration equilibrium constant, K_{hydr} (2), the water vapour partial pressure, p_{H_2O}, and the effective acceptor concentration, $[X'_{Ce,eff}]$:

$$[OH_O^{\bullet}] = \frac{-6K_{hydr}p_{H_2O} + \left(36K_{hydr}^2 p_{H_2O}^2 - 16K_{hydr}p_{H_2O}[X'_{Ce,eff}]^2 + 96K_{hydr}p_{H_2O}[X'_{Ce,eff}] + 4K_{hydr}^2 p_{H_2O}^2[X'_{Ce,eff}]^2 - 24K_{hydr}^2 p_{H_2O}^2[X'_{Ce,eff}]\right)^{\frac{1}{2}}}{8 - 2K_{hydr}p_{H_2O}} \tag{8}$$

It should be noted that (8) does not account for any associations between the positively charged defects ($v_O^{\bullet\bullet}$ or $OH_O^{\bullet}$) and the acceptors. This is done intentionally to both limit the number of fitting parameters, to $\Delta_{hydr}H^{\circ}$, $\Delta_{hydr}S^{\circ}$ and $[X'_{Ce,eff}]$, and to adhere with the traditional defect chemical models employed in the literature.

Figure 3 shows the measured proton concentrations of all compositions as a function of reciprocal temperature along with modelled curves generated by fitting the data to (8). Again, the proton concentrations do not reach the saturation level given by the nominal acceptor concentration, even at water vapour partial pressures of 1 atm underpinning a fundamental limitation to further hydration. The modelled curve fits the presented data using the same hydration parameters ($\Delta_{hydr}H^{\circ}$ and $\Delta_{hydr}S^{\circ}$) for all water vapour partial pressures. The uncertainties in $\Delta_{hydr}H^{\circ}$ and $\Delta_{hydr}S^{\circ}$ have been determined by the standard deviation from 3D curve-fitting (not shown).
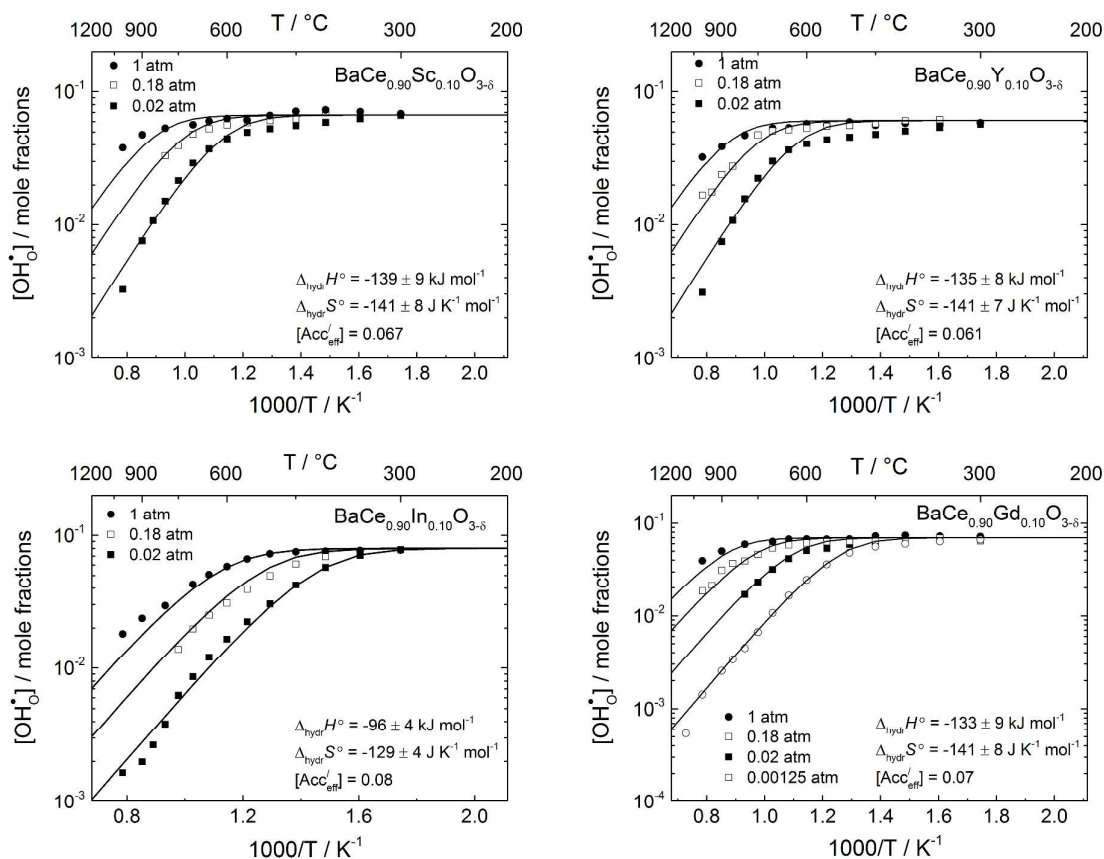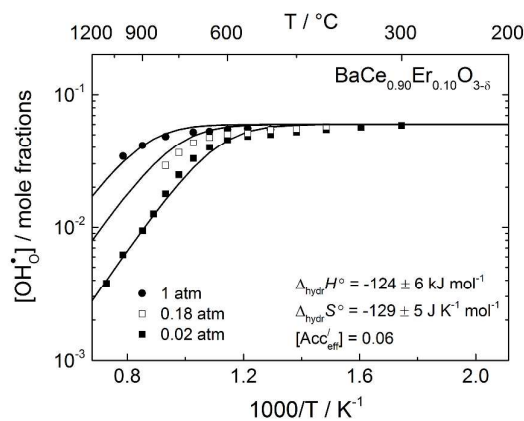
Figure 3: Equilibrium proton concentrations measured by TG of all compositions investigated given in the following order; BCSc10, BCY10, BCIn10, BCGd10 and BCEr10. The solid lines are the curve-fitted proton concentrations.

Fig. 4: Extracted hydration enthalpies from curve-fitting of TG measurements plotted versus the ionic radius (A) and electronegativity (B) of the acceptor dopant. The solid lines represent a linear trendline for all dopants while the dashed lines are the specific values for Ce for reference.

From the empirical correlations between the hydration thermodynamics and the tolerance factors and electronegativity differences[1, 2], the hydration enthalpy should decrease (more exothermic) with increasing ionic radius or decreasing electronegativity of the acceptor as this effectively lowers the tolerance factor and χ_{B-A}, respectively. In Fig. 4, the hydration enthalpies determined from curve-fitting the TG results (Figure 3) are plotted as a function of the ionic radius and electronegativity. For both material parameters, the general trend is consistent with the empirical correlations, but In^{3+} deviates considerably from the linear trendline for the ionic radii. The electronegativity plot is not as clear because the rare-earth acceptors (Er, Gd, Y and Sc) exhibit very similar electronegativities and the result will therefore yield a linear trendline almost regardless of the hydration enthalpy for In. To further assess the validity of the electronegativity correlation, other acceptor dopants with very low or high electronegativities could be included. Unfortunately, these elements typically display a low solubility making them unsuitable for experimental studies: Ga, for instance, has an electronegativity of 1.82 – far higher than all other dopants investigated, but shows limited solubility (see supplementary information). To circumvent this, we turn to DFT calculations allowing us to study a wider range of electronegativities and ionic radii.

4.2. Defect energetics from DFT calculations

To determine the hydration enthalpies from DFT calculations, one needs to account for the stability of protons and oxygen vacancies at the structurally different oxygen lattice sites in the acceptor doped systems. Both these defects were most stable on the 4c site for all dopants (apical position), in correspondence to similar computational work on Gd-doped $BaCeO_3$ by Hermet *et al.*[35]. The relative stability between the isolated point defects and their associated forms; $(X_{Ce}OH_O)^{\times}$ and $(X_{Ce}v_O)^{\bullet}$, is given by their respective association enthalpies. These enthalpies have been calculated by the relative energy differences of the positively charged point defects in their most stable positions close to and far away from the acceptor in the same supercell. Additional calculations taking the formation energy differences between the associates and the isolated point defects yielded similar values. The association enthalpies for all dopants are plotted in Figure 5 as a function of the ionic radius (A) and electronegativity (B) of the acceptor. The dashed vertical line denotes the value for Ce (i.e. undoped $BaCeO_3$) for comparison. As the figure demonstrates, all association energies are exothermic, indicating that these associated defect pairs will be favoured over the isolated point defects at lower temperatures, in line with corresponding work on similar perovskite oxides[14, 19-21, 35]. It

can also be noted that a larger difference in either the electronegativity or the ionic radius between the host and the acceptor generally results in more exothermic association enthalpies. This type of trend for the association enthalpies has also been demonstrated for acceptor doped $BaZrO_3$[36] and $BaSnO_3$[37].
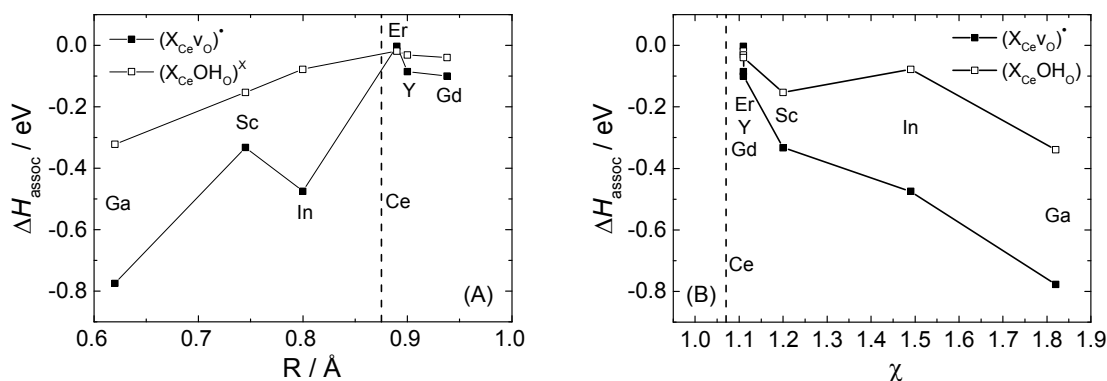

Figure 5: Association enthalpies between the acceptor and oxygen vacancies or protons calculated by DFT as a function of ionic radius (A) and electronegativity (B) for the acceptor.

While the associated pairs will dominate over the isolated oxygen vacancies and protons at lower temperatures for all acceptor dopants, free oxygen vacancies and protons may still co-exist along with the associated defect pairs. Oxygen vacancies and complexes of oxygen vacancies and acceptors will, as such, both hydrate to form protons. Figure 6A shows the calculated hydration enthalpies for oxygen vacancies directly coordinated to or far away from the acceptor as determined using (4) and (5) along with the hydration enthalpies determined experimentally in Figure 6B for comparison. There are several points to address from this figure: The hydration enthalpy for unassociated oxygen vacancies to form unassociated protons determined by DFT calculations gave the same values for all dopants investigated (-116 kJ/mol). Thus, if only the isolated oxygen vacancies hydrate, the hydration energetics are unlikely to change much by varying the type of dopant. This is, however, contradictory to the enthalpies determined by TG measurements (Figure 6B) as well as other experimental work showing different hydration properties when changing the dopant[4-6]. Consequently, the results presented here could suggest that the hydration energetics for certain dopants such as In are dominated by associate complexes. The hydration enthalpies from DFT calculations are nonetheless consistently calculated from the oxygen vacancy and acceptor associates. The

figure otherwise demonstrates that the enthalpies determined by DFT calculations are similar to the values determined by TG measurements with the latter values being slightly more exothermic for all dopants. The DFT calculations moreover reveal that, when also accounting for Ga, the hydration enthalpies exhibit a non-linear dependency with respect to the electronegativity of the acceptor underlining the need for further insight into material specific properties to elucidate the variations in the hydration enthalpy upon changing dopant. It is important to note that without the inclusion of Ga, the remaining dopants show an apparent linear trend as a function of the acceptor electronegativity for both the TG measurements and the DFT calculations, which could easily cause misinterpretations.
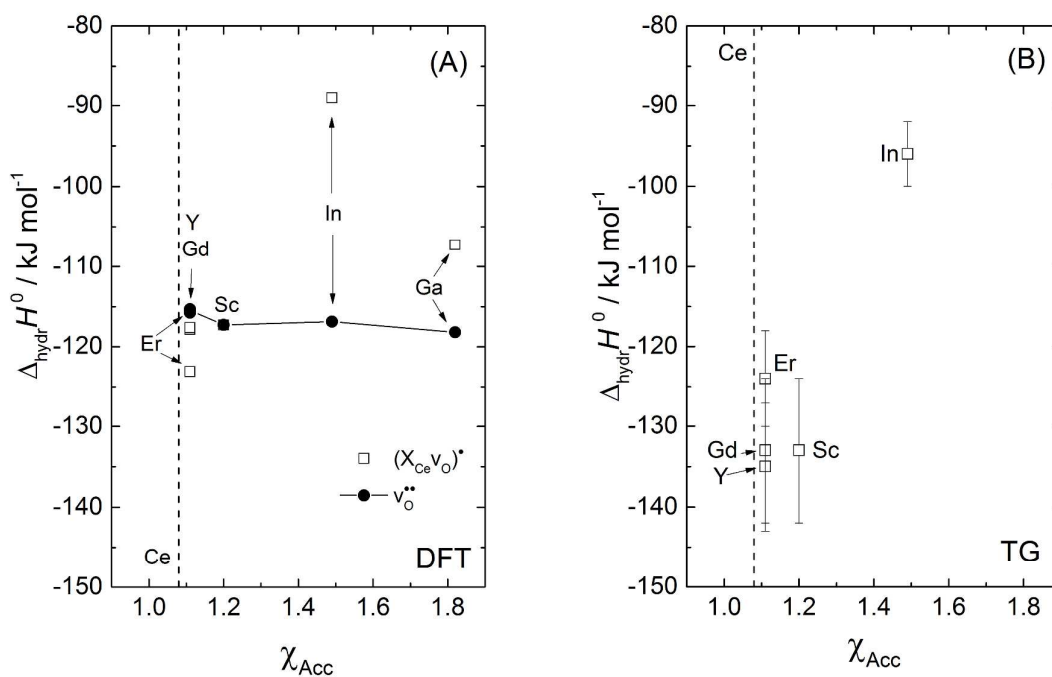

Figure 6A: Hydration enthalpies of unassociated and associated oxygen vacancies, closed and open symbols, respectively, as calculated by DFT as a function of the electronegativity of the acceptor. B displays the hydration enthalpies determined experimentally from TG measurements for comparison. The dashed line indicates the electronegativity for Ce for reference.

5. Discussion

Trends in hydration thermodynamics

To explain the limitations of the proposed empirical correlations, and specifically why In^{3+} deviates considerably, further details of the ionic character of the bonds in the specific material systems are needed. The ionic character can for instance be investigated in terms of the Bader charges of the constituent ions. This approach is advantageous because it relies entirely on the electron density separating individual ions by maxima/minima in electron density volume distributions. The enclosed Bader volumes will then result in effective charges of the specific ions. While the formal charges of the different acceptors should be equal, the differences in the effective Bader charges will yield specific information about the ionic character of the materials' bonds. Table 2 presents the Bader charges of X, O4cx and O8dx in the order of increasing electronegativity of the acceptor. Bader charges of Ba, Ce, O4c and O8d have not been included as their values were approximately the same throughout the dopant systems studied. The oxide ions closer to the dopant (O4cx and O8dx) are consistently more negative than the bulk oxide ions (O4c and O8d), where the latter exhibit values of -1.26 and -1.25, respectively. The O4cx ions are slightly more negative than the O8dx ions, which explains the inclination for oxygen vacancies and protons to be more stable at the O4cx sites. Lastly, oxide ions around the rare earth cations (Gd^{3+}, Sc^{3+}, Y^{3+}, Er^{3+}) are consistently more negative than oxide ions around the p-block cations (Ga^{3+} and In^{3+}) indicating a more ionic character of the X-O bond for the rare earth cations. Figure 7 shows the hydration enthalpies determined by DFT calculations and TG measurements as a function of the Bader charge of the oxygen ions closest to the dopant (O4cx and O8dx). While there are some minor differences in the hydration enthalpies determined by the two techniques, the general trends are preserved with In^{3+} yielding the least exothermic enthalpy (DFT: -89 kJ mol^{-1}, TG: -96 kJ mol^{-1}). The hydration enthalpy clearly becomes increasingly negative with more negative oxide ions, suggesting that the hydration enthalpies become more exothermic with an increasing ionic character of the X-O bond.

Table 2: Bader charges of the dopant (X) and the oxide ions directly coordinated to X in the Wyckoff positions 4c and 8d, O4cx and O8dx, respectively.

Dopant	X	O4cx	O8dx	χ (Allred-Rochow)
Y^{3+}	2.13	-1.32	-1.31	1.11
Gd^{3+}	2.17	-1.32	-1.32	1.11
Er^{3+}	2.23	-1.34	-1.33	1.11
Sc^{3+}	2.02	-1.31	-1.31	1.20
In^{3+}	1.82	-1.28	-1.28	1.49
Ga^{3+}	1.82	-1.29	-1.29	1.82

The choice of dopant is thus directly responsible for the hydration thermodynamics and the more covalent character of the In-O bond demonstrated here may similarly be responsible for the low exothermic hydration enthalpies shown for In-doped $BaZrO_3$ and $BaSnO_3$[4, 38]. A detailed study of the bond strength and ionic character of dopant-oxygen bonds in different material systems will be pursued to further elaborate on the hydration trends discussed here.
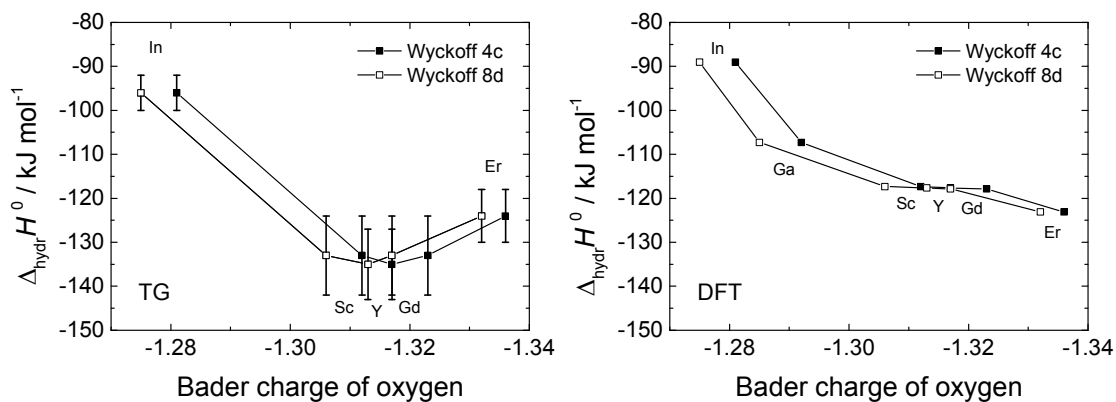

Figure 7: Hydration enthalpies evaluated by curve-fitting TG curves (left) and by DFT calculations (right) plotted as a function of the oxygen Bader charge closest to the dopant. Bader charges have been determined by DFT calculations.

16

Limited proton concentrations

All included compositions displayed lower proton uptake than that expected from their nominal acceptor concentration (10 atomic %) (cf. Figure 3). A lower dopant solubility than 10 atomic% in $BaCeO_3$ can first of all be neglected as a potential explanation since XRD and SEM showed that all compositions studied were single phase (see supplementary information for more details). To assess the extent of BaO evaporation, which can result in dopant incorporation on the A-site, selected compositions (BCY10 and BCIn10) were exposed to isothermal dwells up to 5 hours at 1400 °C, i.e. 100 °C higher than the annealing temperature. Both compositions retained their level of saturation after the heat treatment (not shown) indicating that the processing conditions employed have not resulted in any significant dopant incorporation on the A-site.

DFT results indicate that there is a tendency for protons and oxygen vacancies to associate with X at lower temperatures forming associate pairs (cf. Figure 5). The acceptors can also form larger complexes with the positive defects e.g. $(X_{Ce}v_OX_{Ce})^X$ or $(X_{Ce}OH_OX_{Ce})^/$, which could limit complete hydration in a frozen-in situation at lower temperatures. As these acceptor configurations require the dopants to be mobile, they will only form at higher temperatures during synthesis, as the temperature range employed for all measurements (T ≤ 1100 °C) is unlikely to result in any significant cation diffusion. The extent of formation of these complexes can be explored by combining the formation enthalpies of $v_O^{\bullet\bullet}$ and $OH_O^{\bullet}$, with the association enthalpies of the $(X_{Ce}v_O)^{\bullet}$, $(X_{Ce}OH_O)^{\times}$, $(X_{Ce}v_OX_{Ce})^{\times}$, $(X_{Ce}OH_OX_{Ce})^/$ and $(X_{Ce}OH_OX_{Ce}OH_O)^{\times}$ complexes, from DFT calculations along with the complete electroneutrality condition:

$$2[v_O^{\bullet\bullet}] + [OH_O^{\bullet}] + [(X_{Ce}v_O)^{\bullet}] = [X_{Ce,free}^/] + [(X_{Ce}OH_OX_{Ce})^/] \tag{9}$$

where $[X_{Ce,free}^/]$ is the unassociated acceptor concentration. Further details are given in the supplementary information.

The resulting defect concentrations under wet conditions ($p_{H_2O} = 0.025$ atm) for BCIn10 and BCSc10 are presented in Figure 8 as a function of temperature. The other compositions

showed similar defect concentration profiles. The proton acceptor complexes, $(X_{Ce}OH_O)^\times$, $(X_{Ce}OH_OX_{Ce})^/$ and $(X_{Ce}OH_OX_{Ce}OH_O)^\times$, have been omitted as their concentrations are minute in the temperature range (800-1600 °C) presented. The figure demonstrates that a significant fraction of the incorporated acceptor can be trapped in $(X_{Ce}v_OX_{Ce})^\times$ complexes, depending on the processing temperature employed. Therefore, while lowering the calcination or sintering temperatures may be beneficial in terms of lowering Ba-deficiency, it will result in larger concentrations of oxygen vacancy and acceptor complexes. To assess whether such complexes will affect the proton uptake, two additional BCIn10 compositions were synthesised by a single calcination at 1400 and 1600 °C for 12 h. The synthesis procedure and materials characterisation were otherwise the same as described in the supplementary information. The resulting proton concentrations determined by TG measurements of the samples calcined at maximum temperatures between 1300 and 1600 °C are presented in Fig. 9. As the figure demonstrates, BCIn10 displays higher proton concentrations with increasing synthesis temperatures approaching $[OH_O^\bullet] = 0.1$ mole fractions when calcined at 1600 °C. This indicates that the $(X_{Ce}v_OX_{Ce})^\times$ complexes are responsible for the limiting proton uptake in acceptor doped $BaCeO_3$ and as such, all compositions should ideally be synthesised at the highest temperatures attainable to avoid the formation of $(X_{Ce}v_OX_{Ce})^\times$ allowing higher levels of proton concentrations. It should also be noted that the presence of these complexes will undoubtedly influence both the transport properties and hydration thermodynamics of acceptor doped $BaCeO_3$. For instance, the $(X_{Ce}v_OX_{Ce})^\times$ configurations that are frozen-in during synthesis will severely trap protons due to the more negative association enthalpies of the $(X_{Ce}OH_OX_{Ce})^/$ complexes. In the case of Gd-doped $BaCeO_3$, the $(Gd_{Ce}OH_O)^\times$ complex displays an association enthalpy of -0.13 eV, while that of $(Gd_{Ce}OH_OGd_{Ce})^/$ with respect to the $(Ce_{Ce}O_OCe_{Ce})^{//}$ configuration is -0.41 eV. As a result, the effective enthalpy of the proton mobility will increase, yielding significantly lower proton conductivities. Also, the experimentally determined hydration thermodynamics will depend on the complexes that are formed. The use of simultaneous TG-DSC, which measures reaction enthalpies directly, could therefore be a valuable tool to distinguish the different hydration mechanisms[3, 24]. Further work elucidating the extent of complex formation and its effect on the hydration mechanisms, proton uptake and transport properties is thus called upon to address these matters in more detail.
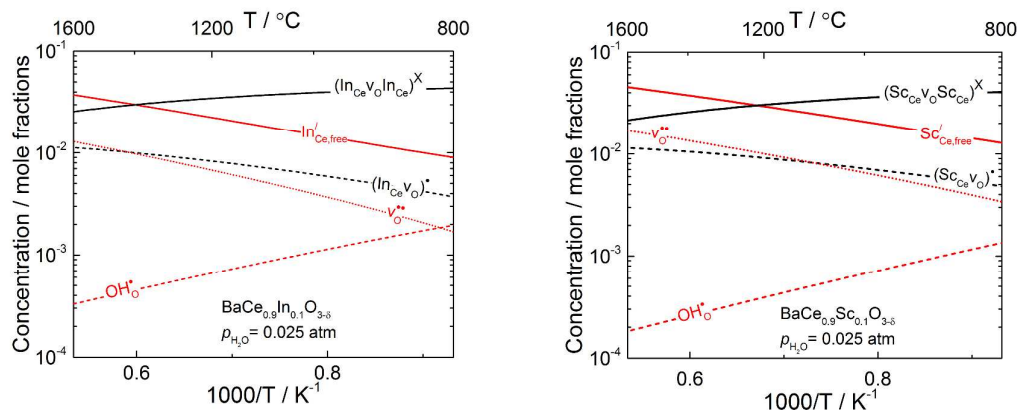
Figure 8: Equilibrium defect concentrations for all defects considered in this work for BCIn10 and BCSc10 using thermodynamics determined by DFT calculations as a function of temperature under wet conditions (p_{H_2O} = 0.025 atm).
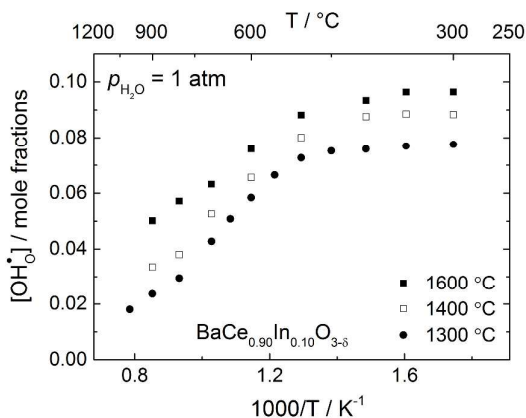

Figure 9: Equilibrium proton concentrations determined by TG for three different samples of BCIn10 calcined at 1300, 1400 and 1600 °C for 12 hours.

Conclusion

In this contribution, the effect of the choice of dopant on the thermodynamics of hydration and complex formation in $BaCe_{0.9}X_{0.1}O_{3-\delta}$ (X = Sc, Ga, Y, In, Gd and Er) has been investigated. Comprehensive and extensive thermogravimetric (TG) measurements and first principles calculations (DFT), have in combination, allowed a wider range of acceptor dopants to be investigated and assessed. The results from both approaches are in excellent

19

agreement and demonstrate that the hydration enthalpy depends on the ionic character of the dopant-oxygen bond. The enthalpy becomes more exothermic with increasing ionic character, varying from -96 kJ mol^{-1} to -135 kJ mol^{-1} as determined by TG measurements. Complexes between the negatively charged acceptors and positively charged oxygen vacancies, or protons, are shown to dominate the defect structure of all compositions. Such complexes will therefore play a significant role in the hydration and transport properties, and different processing conditions will yield large variations in the specific defect concentrations. Further, the association enthalpies for acceptors and oxygen vacancies, or protons, generally become increasingly negative when the difference in the ionic radius or electronegativity between the acceptor and host cation (Ce^{4+}) increases, thereby resulting in larger concentrations of complexes. This can for instance have severe implications on the proton conductivity as the activation energies will be significantly higher. Larger complexes have also been investigated and are demonstrated to be a direct cause for limiting proton concentrations where the acceptors trap oxygen vacancies to a larger extent than protons. Raising the synthesis temperature is proposed as a way to inhibit the formation of complexes and increase the level of protons in these materials.

Acknowledgements

References

1.   T. Norby, M. Widerøe, R. Glöckner and Y. Larring, *Dalton Transactions*, 2004, 3012-3018.

2.   T. S. Bjørheim, A. Kuwabara, I. Ahmed, R. Haugsrud, S. Stølen and T. Norby, *Solid State Ionics*, 2010, **181**, 130-137.

3.   A. Løken, C. Kjølseth and R. Haugsrud, *Solid State Ionics*, 2014, **267**, 61-67.

4.   K. D. Kreuer, S. Adams, W. Münch, A. Fuchs, U. Klock and J. Maier, *Solid State Ionics*, 2001, **145**, 295-306.

5.   M. Oishi, S. Akoshima, K. Yashiro, K. Sato, T. Kawada and J. Mizusaki, *Solid State Ionics*, 2010, **181**, 1336-1343.

6.   M. Oishi, S. Akoshima, K. Yashiro, K. Sato, J. Mizusaki and T. Kawada, *Solid State Ionics*, 2009, **180**, 127-131.

7.   J. F. Liu and A. S. Nowick, *Solid State Ionics*, 1992, **50**, 131-138.

8.   A. Kruth and J. T. S. Irvine, *Solid State Ionics*, 2003, **162–163**, 83-91.

9.   D. Shima and S. M. Haile, *Solid State Ionics*, 1997, **97**, 443-455.

10.   D. A. Stevenson, N. Jiang, R. M. Buchanan and F. E. G. Henn, *Solid State Ionics*, 1993, **62**, 279-285.

11.   K. D. Kreuer, *Solid State Ionics*, 1999, **125**, 285-302.

12.   S. M. Haile, D. L. West and J. Campbell, *Journal of Materials Research*, 1998, **13**, 1576-1595.

13.   J. Wu, R. A. Davies, M. S. Islam and S. M. Haile, *Chemistry of Materials*, 2005, **17**, 846-851.

14.   M. S. Islam, P. R. Slater, J. R. Tolchard and T. Dinges, *Dalton Transactions*, 2004, DOI: 10.1039/B402669C, 3061-3066.

15.   K. D. Kreuer, *Annual Review of Materials Research*, 2003, **33**, 333-359.

16.   F. Krug and T. Schober, *Journal of the American Ceramic Society*, 1997, **80**, 794-796.

17.   H. Uchida, H. Yoshikawa and H. Iwahara, *Solid State Ionics*, 1989, **35**, 229-234.

18.   Y. Okuyama, T. Kozai, T. Sakai, M. Matsuka and H. Matsumoto, *Electrochimica Acta*, 2013, **95**, 54-59.

19.   S. J. Stokes and M. S. Islam, *Journal of Materials Chemistry*, 2010, **20**, 6258-6264.

20.   Y. Yamazaki, F. Blanc, Y. Okuyama, L. Buannic, J. C. Lucio-Vega, C. P. Grey and S. M. Haile, *Nat Mater*, 2013, **12**, 647-651.

21.   M. A. Gomez and F.-J. Liu, *Solid State Ionics*, 2013, **252**, 40-47.

22.   T. Matzke, U. Stimming, C. Karmonik, M. Soetratmo, R. Hempelmann and F. Güthoff, *Solid State Ionics*, 1996, **86–88, Part 1**, 621-628.

23.   F. Giannici, A. Longo, A. Balerna, K. D. Kreuer and A. Martorana, *Chemistry of Materials*, 2007, **19**, 5714-5720.

24.   C. Kjølseth, L.-Y. Wang, R. Haugsrud and T. Norby, *Solid State Ionics*, 2010, **181**, 1740-1745.

25.   S. Ricote, N. Bonanos and G. Caboche, *Solid State Ionics*, 2009, **180**, 990-997.

26.   K. D. Kreuer, *Solid State Ionics*, 1999, **125**, 285-302.

27.   R. D. Shannon, *Acta Crystallographica Section A*, 1976, **32**, 751-767.

28.   E. J. Little and M. M. Jones, *Journal of Chemical Education*, 1960, **37**, 231.

29.   G. Kresse and J. Furthmüller, *Physical Review B*, 1996, **54**, 11169-11186.

30.   J. P. Perdew, K. Burke and M. Ernzerhof, *Physical Review Letters*, 1996, **77**, 3865-3868.

31.   G. Kresse and D. Joubert, *Physical Review B*, 1999, **59**, 1758-1775.

32.   R. Hempelmann, M. Soetratmo, O. Hartmann and R. Wäppling, *Solid State Ionics*, 1998, **107**, 269-280.

33.   G. Henkelman, A. Arnaldsson and H. Jónsson, *Computational Materials Science*, 2006, **36**, 354-360.

34.   M. Oishi, K. Yashiro, K. Sato, J. Mizusaki, N. Kitamura, K. Amezawa, T. Kawada and Y. Uchimoto, *Solid State Ionics*, 2008, **179**, 529-535.

35.   J. Hermet, F. Bottin, G. Dezanneau and G. Geneste, *Physical Review B*, 2012, **85**, 205137.

36.   M. E. Björketun, P. G. Sundell and G. Wahnström, *Physical Review B*, 2007, **76**, 054307.

37.   É. Bévillon, J. Hermet, G. Dezanneau and G. Geneste, *Journal of Materials Chemistry A*, 2014, **2**, 460-471.

38.   Y. Wang, A. Chesnaud, E. Bevillon, J. Yang and G. Dezanneau, *International Journal of Hydrogen Energy*, 2011, **36**, 7688-7695.